Nanoscale

PAPER

View Article Online
View Journal | View Issue

Cite this: *Nanoscale*, 2017, **9**, 3476

Antiferromagnetic interlayer coupling and thus induced distinct spin texture for the $[LaMnO_3/LaCoO_3]_5$ superlattices†

Jing Zhang, Hongrui Zhang, Xuejing Zhang, Xiangxiang Guan, Xi Shen, Deshun Hong, Hui Zhang, Banggui Liu, Richeng Yu, Baogen Shen and Jirong Sun*

Received 28th November 2016,
Accepted 12th February 2017

DOI: 10.1039/c6nr09242j

rsc.li/nanoscale

Artificial engineering of an interfacial spin structure of complex oxides with strongly coupled spin, orbital, charge and lattice degrees of freedom is crucially important for the exploration of novel effects associated with magnetic tunneling, exchange biasing, and spin injecting/manipulating, which are the central issues of spintronics. Here we demonstrate the presence of a distinct interlayer coupling between $LaMnO_3$ (LMO) and $LaCoO_3$ (LCO) and the resulting dramatic effect on the spin structure. We found that the LCO layer in $(LMO/LCO)_5$ superlattices exhibits not only an antiferromagnetic coupling with a neighboring LMO layer but also a long-range magnetic order with substantially reduced magnetization. As suggested by density functional theory calculations, interlayer coupling can induce a spatial oscillation of magnetic moment within the LCO layer, resulting in low magnetization.

1. Introduction

Because of interlayer coupling, spatial confinement, and charge/orbital reconstruction, complex oxide interfaces are distinct from bulk materials,[1] exhibiting a number of novel effects, such as two-dimensional superconductivity[2,3] and interfacial ferromagnetism[4–6] for the $LaAlO_3/SrTiO_3$ interface, enhanced ferromagnetic (FM) order for the $La_{0.7}Sr_{0.3}MnO_3/BaTiO_3$ superlattices (SLs),[7] antiferromagnetic (AFM) interlayer coupling for the $La_{0.7}Sr_{0.3}MnO_3/SrRuO_3$ (LSMO/SRO) SLs[8] and bilayers,[9] and distinct magnetic order in paramagnetic (PM) layers for the $YBa_2Cu_3O_{7-\delta}/La_{0.7}Ca_{0.3}MnO_3$ [10–12] and $LaNiO_3/LaMnO_3$ (LNO/LMO)[13] SLs. Among these, the latter phenomenon is particularly interesting in a sense that it demonstrated the induction of a well-defined spin texture in the PM layers by a neighboring FM layer. As experimentally revealed, spins of the Cu ions in the interfacial layer of $YBa_2Cu_3O_{7-\delta}$ prefer to align against those of the Mn ions of $La_{0.7}Ca_{0.3}MnO_3$, leading to strong magnetic proximity effects.[12] These results are different from those obtained for the FM/FM type bilayers, for which interlayer coupling does not affect the spin texture within each layer though sometimes it causes an AFM ordering of the two neighboring FM layers as in the LSMO/SRO superlattices[8] and bilayers.[9]

Herein we are interested in the SLs composed of $LaCoO_3$ (LCO) and LMO. LCO is attractive for its sensitivity to external perturbations, due to the strong competition between Hund's rule coupling and crystal field splitting. As is well documented in the literature, bulk LCO is nonmagnetic at low temperatures, *i.e.*, the Co^{3+} ions are in the low spin (LS) state with zero magnetic moment (t_{2g}^6, $S = 0$). However, when the temperature is increased to above 110 K, LCO gradually evolves into a PM state: thermal excitation has driven the LS Co^{3+} ions to an intermediate spin (IS) state with nonzero magnetic moment ($t_{2g}^5e_g^1$, $S = 1$).[14,15] The spin state can also be tuned by lattice strains:[16] parts of the LS Co^{3+} ions were pushed into the high spin (HS) state ($t_{2g}^5e_g^1$, $S = 2$) by tensile strain, forming a long range FM order mediated by the superexchange.[17] Physical[18] and chemical[19] pressure, even photoexcitation[20] also have strong effects on the spin state. Different from LCO, LMO stays in an A-type AFM ground state when it is orthorhombic[21] or a FM state when it is tetrahedral. Tetrahedral structural distortion has depressed the cooperative Jahn–Teller distortion, favoring the FM order.[22,23] Notably, both LCO and LMO are insulators, and their magnetism arises mainly from superexchange. This is different from the LSMO/SRO SLs. As is well known, LSMO and SRO are metallic perovskites for which electrical conduction is required to generate the double exchange (for LSMO) or itinerant FM exchange (for SRO). Here we report on the discovery of an AFM LMO/LCO interlayer coupling and its effect on the spin texture for the $(LMO/LCO)_5$ SLs. Due to

Beijing National Laboratory for Condensed Matter & Institute of Physics, Chinese Academy of Sciences, Beijing 100190, People's Republic of China. E-mail: jrsun@iphy.ac.cn

†Electronic supplementary information (ESI) available. See DOI: 10.1039/c6nr09242j

the simultaneous occurrence of AFM interlayer coupling and associated lattice modulation, the LCO layer in SLs exhibits a long-range magnetic order with significantly reduced magnetization. As suggested by the calculation of density functional theory, spatial spin oscillation may take place within the LCO layer. The present work opens an approach towards spin structure engineering for complex oxides.

2. Experimental

SLs with alternatively stacked LMO and LCO layers were grown on (001)-orientated $La_{0.3}Sr_{0.7}Al_{0.65}Ta_{0.35}O_3$ (LSAT) and $SrTiO_3$ (STO) substrates ($3 \times 5 \times 0.5$ mm^3) by the pulsed laser ablation technique at the substrate temperature of 720 °C and the oxygen atmosphere of 30 Pa. The adopted laser fluence was 2 J cm^{-2} and the repetition rate was 1 Hz (KrF excimer laser, 248 nm). To calibrate the deposition rate, we first prepared LMO and LCO films with a thickness of about 20–30 nm, and then determined the actual film thickness by small angle X-ray reflectivity (ESI, Fig. S1†). In this way, two relationships between layer thickness and pulse number were established for LCO and LMO, respectively. Based on these relationships, the nominal layer thickness of the SLs can be determined *via* tuning the pulse number. All SL samples were prepared in the same batch to obtain perfect regularity.

Fixing the layer thickness of LCO to ~11 unit cells (uc) and varying the LMO layer from ~4 uc to ~24 uc and *vice versa*, two series of SLs with the stacking periodicity of 5 were obtained. To explore the effect of thick/thick layer combination, two more SLs of 16/16 uc (LMO/LCO) and 24/24 uc (LMO/LCO) were also prepared. Hereafter, the SLs will be denoted as LMO(t_1)/LCO(t_2), where t_1 and t_2 are layer thicknesses in the unit of unit cell. For all of the SLs, the bottom and top layers are LCO and LMO, respectively.

To determine the actual layer thickness of the SLs, we performed a systematic analysis of the high-angle annular dark field (HAADF) images for a series of SL samples on STO with the nominal LCO layer thickness of 2.1, 4.2, 8.4, and 12.6 nm and a fixed LMO layer of 5.7 nm. Through directly counting the uc numbers of the LMO and LCO layers, we established a conversion relationship between nominal and actual layer thickness (ESI, Fig. S2†). The actual layer thickness is slightly thinner than the nominal one. All of the layer thicknesses presented here were actual thicknesses. The layer thickness thus obtained suffered from an uncertainty of ±1 uc due to the slight overlap of the energy-dispersive X-ray spectroscopy (EDX) images of Mn and Co at the LMO/LCO interface (not shown).

The surface morphology of the SLs was measured by using an atomic force microscope (AFM, SPI 3800N, Seiko). The crystal structure of the films was determined by using a Bruker diffractometer (D8 Discover, Cu K_α radiation). Lattice images were recorded by using a high-resolution aberration-corrected scanning transmission electron microscope with double C_S correctors for the condenser lens and objective lens (STEM, JEM-ARM200F). Magnetic measurements were conducted in the temperature interval from 5 K to 300 K by using a Quantum Designed Vibrating Sample Magnetometer (VSM-SQUID) with in-plane magnetic fields.

3. Results and discussion

The inset images in Fig. 1a and b present the typical surface morphologies of [LMO(11)/LCO(8)]$_5$/STO and [LMO(11)/LCO(8)]$_5$/LSAT, respectively. Terrace-featured topography indicates a two-dimensional growth for the film above STO. The root mean square roughness is ~0.2 nm, irrespective of the layer thickness. Although an island-like growth mode is observed for the SLs on LSAT, the film surface is still rather flat, and the root mean square roughness varies between ~0.2 nm and ~0.8 nm, enhancing with layer thickness. The slightly increased surface roughness may be ascribed to the large lattice mismatch between LMO and LSAT (3.91 Å *versus* 3.86 Å).

The main panel of Fig. 1a shows a HAADF image of the cross section of [LMO(11)/LCO(8)]$_5$/STO, here the brighter atomic columns correspond to La and the fainter columns correspond to Mn or Co. SLs exhibit a coherent growth on the substrate. Fascinatingly, parallel dark stripes are formed in a lattice image, appearing in every other column in parallel to the interface. A quantitative analysis indicates that the La–La space is 4.26 Å in a dark stripe and 3.28 Å elsewhere, and the average La–La distance is 3.77 Å. Because of the similar atomic number of Mn and Co, the LMO–LCO interface is not clear. EDX analysis shows that the atomic layers with parallel dark stripes are LCO (not shown). This is a usual result since the single LCO layer on STO prefers perpendicular stripes due to in-plane tensile strains as reported by different groups.[24,25] Notably, parallel dark stripes are a general feature of the lattice image of the LMO/LCO SLs, observed in the SLs not only on STO but also on LSAT as long as the LCO layer is thick enough ($t_2 \geq 8$ uc) (Fig. 1b). Possibly, for SLs the elastic energy associated with lattice strains is no longer the only driving force for structural modulation, and the magnetic energy gained from the LMO–LCO interlayer coupling, the occurrence of which will be shown later, may be also at play, stabilizing the IS/HS state of the Co^{3+} ions along the LCO–LMO interface. This analysis is consistent with the observation that the first row in proximity of LMO is usually a dark stripe (not shown).

In Fig. 2a we show the X-ray diffraction (XRD) patterns of [LMO(11)/LCO(24)]$_5$/LSAT. Besides the main (002) reflection, satellite peaks corresponding to the SL structure (marked by above numbers) and the finite-size oscillations due to finite layer thickness (marked by triangles) can be clearly seen, signaling a high quality of the specimen. Similar XRD spectra with slightly different details are obtained for other SL samples (ESI, Fig. S3†). As a representative, the out-of-plane lattice constant of LMO(11)/LCO(t_2) is shown in Fig. 2b, as a function of layer thickness of LCO. It exhibits a monotonic decrease with t_2, which is reasonable noting the small lattice

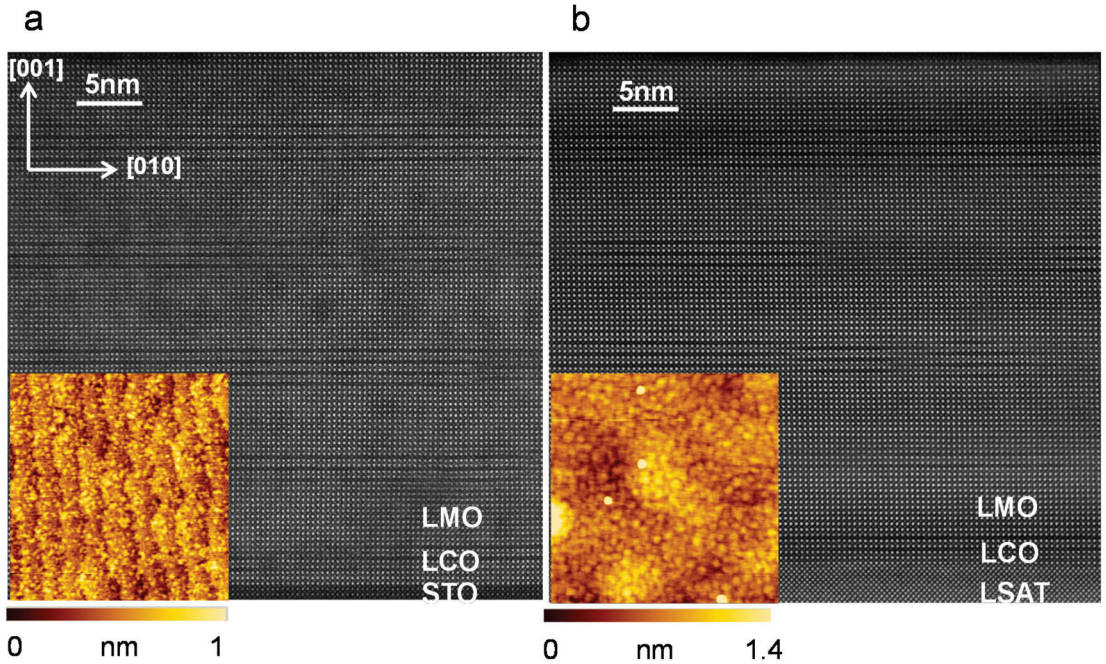

Fig. 1 High-angle annular dark field (HAADF) images of the cross sections of $[LMO(11)/LCO(8)]_5$/STO (a) and $[LMO(11)/LCO(8)]_5$/LSAT (b). Brighter and fainter atomic columns correspond to La and Mn or Co, respectively. Atomic layers with parallel dark stripes are LCO. Inset images in (a) and (b) are the surface morphologies of the corresponding samples ($1 \times 1\ \mu m^2$), measured by using an atomic force microscope.

constant of LCO compared with LMO (3.82 Å (ref. 26) *versus* 3.91 Å (ref. 27)).

Based on a simple formula

$$c = \frac{t_1}{t_1 + t_2} c_{LMO} + \frac{t_2}{t_1 + t_2} c_{LCO},$$

the experimental relationship can be well reproduced with appropriate c_{LMO} and c_{LCO}, the lattice parameters of the LMO and LCO layers, respectively. The solid curves in Fig. 2b show the results of data fitting with the parameters marked beside each curve (c_{LMO}, c_{LCO}). Compared with the bulk value, the lattice constant of the LCO layer is considerably small, ~3.779 Å on LSAT and ~3.745 Å on STO, manifesting tensile strains within the layer. In contrast, the LMO layer is slightly compressive, as indicated by enlarged *c*-axis lattice constants.

To get further information on lattice strains, the reciprocal space mapping (RSM) of the ($\bar{1}03$) reflection was measured. Fig. 2c exemplifies the RSM of $[LMO(11)/LCO(24)]_5$/LSAT. A remarkable feature is the vertical alignment for the reflections of the SLs and the substrate. It means that the SLs share the same in-plane lattice constant with a substrate. Although the SLs are as thick as ~70 nm, there are no visible lattice relaxations. This conclusion is also true for the SLs grown on STO (ESI, Fig. S3†). From the deduced lattice constants, the cell volumes of the SLs can be calculated. They are ~57.4 $Å^3$ and ~58.1 $Å^3$ for the LMO(11)/LCO(24) SLs on LSAT and STO, respectively. From LSAT to STO, cell volume is expanded by ~1.2%.

Fig. 3a displays the temperature-dependent magnetization (*M*–*T* relation) of $[LMO(11)/LCO(t_2)]_5$/STO, measured with an

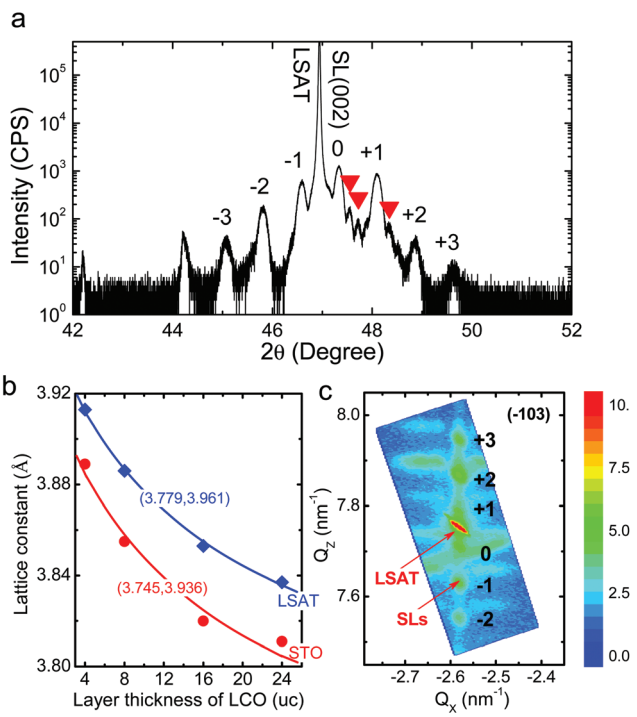

Fig. 2 (a) X-ray diffraction patterns of $[LMO(11)/LCO(24)]_5$/LSAT. Satellite peaks corresponding to the superlattice structure (marked by numbers) and finite-size oscillations arising from finite film thickness (marked by red triangles) can be clearly seen. (b) Out-of-plane lattice constant of $[LMO(11)/LCO(t_2)]_5$, as a function of the layer thickness of LCO. (c) Reciprocal space mapping (RSM) of the (–103) reflection of $[LMO(11)/LCO(24)]_5$/LSAT. The vertical alignment for the reflections of the SL and the substrate indicates that the SL shares the same in-plane lattice constant with the substrate.

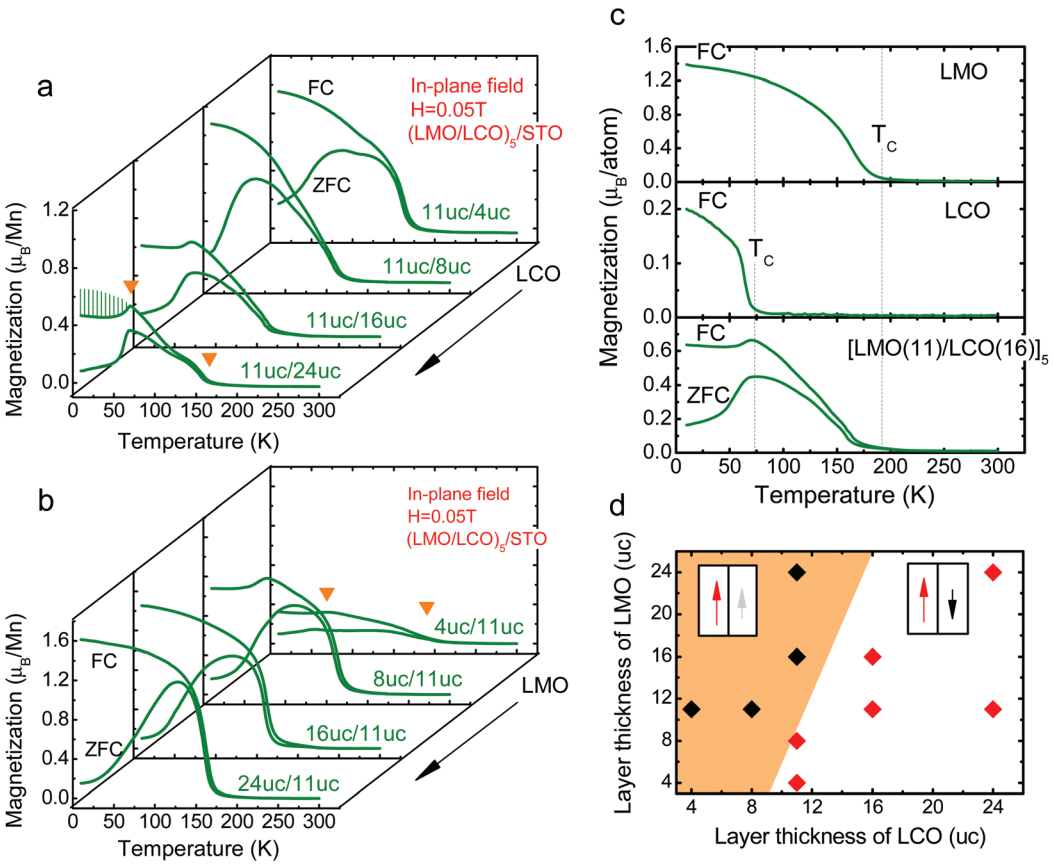

Fig. 3 (a) Temperature dependence of the magnetization of [LMO(11)/LCO(t_2)]$_5$/STO, measured under an applied field of 0.05 T. Only one PM–FM transition is observed at 175 K when $t_2 \leq 8$ uc, and two phase transitions are seen at ~75 K and ~175 K, respectively, when t_2 exceeds 16 uc. ZFC and FC represent zero-field-cooling and field-cooling, respectively. Orange triangles mark the temperature for magnetic transitions. (b) Temperature dependence of the magnetization of [LMO(t_1)/LCO(11)]$_5$/STO, recorded under a field of 0.05 T. Orange triangles mark the temperature for magnetic transitions. (c) A comparison of the magnetic behaviors of the SLs and the corresponding single layers, measured under a field of 0.05 T. (d) A phase diagram on the t_1–t_2 plane. Symbols here represent the thicknesses of the LMO and LCO layers in SLs. Two kinds of symbols mark two different magnetic couplings. Grey arrow denotes the unclear spin state of the LCO layer.

in-plane field of 0.05 T. Here the difference of the two *M*–*T* curves measured by the field-cooling (FC) and zero-field-cooling (ZFC) modes can be ascribed to magnetic inhomogeneity of the LCO layer. A behavior similar to that of LMO was observed when LCO is thin, showing a typical FM transition at ~175 K. When the LCO layer exceeds 16 uc, a second magnetic transition emerges around ~75 K. Unexpectedly, this later phase transition causes a sizable decrease, rather than increase, in magnetization. This feature is especially obvious in LMO(11)/LCO(24), for which a direct estimation gives a magnetic reduction of ~28% (marked by hatched area). This AFM transition-like behavior is also observed when applying an out-of-plane field, indicating that it is not spin reorientation (ESI, Fig. S4†). As will be seen later, this is indicative of an antiparallel alignment of the magnetic moments of LCO and LMO.

By fixing the LCO layer to 11 uc while varying the LMO layer thickness, the evolution of these two-phase transitions can be captured. As illustrated in Fig. 3b, two inflections at ~75 K and ~175 K, respectively, are visible in the *M*–*T* curve when the layer thickness of LMO is 4 uc, signaling the appearance of magnetic anomalies. When the LMO layer thickness is increased from 4 uc to 8 uc, these two anomalies develop into two clear phase transitions. Further increasing the LMO layer up to 16 uc, the low temperature phase transition disappears. Notably, similar behaviors are also observed in the SLs on LSAT (ESI, Fig. S5†), though the lattice strains there are slightly small (the lattice constant is 3.905 Å for STO and 3.860 Å for LSAT). In fact, we also studied the SLs above $LaAlO_3$, which show compressive strains, and observed essentially the same behaviors as those of the former two kinds of SLs (ESI, Fig. S6†).

Comparing the LMO/LCO SLs with their single layer counterparts, we can get further information on phase transition. As shown in Fig. 3c, the two magnetic transitions of the SLs coincide well with those of the two single layers. If the two layers of the SLs keep their single layer properties, the first magnetic transition in SLs can be ascribed to LMO: since LMO has a higher Curie temperature than LCO, its spins will order earlier along the external field when cooled. To explain the magnetic reduction at the second transition, however, a spin

alignment against the magnetic field has to be assumed for LCO. This will happen only when there is an AFM coupling between LMO and LCO.

To get a clear picture on the spin structure, in Fig. 3d we show a phase diagram on the t_1–t_2 plane. Symbols here correspond to the thicknesses of the LMO and LCO layers in SLs. Different phases are marked by different backgrounds. At first glance, an antiparallel spin alignment occurs only in the SLs with relatively thick LCO layers. t_2 = 11 uc is the threshold layer thickness for LCO, below which the magnetic signals of LCO are unidentifiable. The disappearance of the low temperature phase transition in LMO(16)/LCO(11) and LMO(24)/LCO(11) remains unclear at present. Possibly, the signals from the LCO layer which is obviously low are overwhelmed by those of LMO when LMO is thick.

If the spin direction of LCO is antiparallel to an external field, a spin flip is expected under a high enough applied field. This process is indeed observed. Fig. 4a shows the temperature-dependent magnetization of $[LMO(11)/LCO(16)]_5$/STO, measured under different fields in field-cooling mode. Remarkably, the magnetic change at ~75 K undergoes a systematic variation with an applied field, gradually reversing from decrease to increase as the magnetic field grows. A field-induced spin flip is also observed in the SLs on LSAT (ESI, Fig. S6†). These results provide direct evidence for an AFM coupling between LMO and LCO. Simply extrapolating the high temperature part of the M–T curve (>75 K) down to 10 K, the magnetization of the LMO layer can be estimated (solid red symbols in Fig. 4b). For an applied field of 1 T which is nearly the saturation field for our SLs, it is close to the value of the corresponding single layer. From the difference of the measured and extrapolated values, the contribution of the LCO layer can be deduced. It is ~0.20μ_B/Co for LMO(8)/LCO(11), ~0.24μ_B/Co for LMO(11)/LCO(16), and ~0.28μ_B/Co for LMO(11)/LCO(24) at 10 K (solid olive symbols in Fig. 4b). Two series of single layers, LMO and LCO, respectively, are also prepared, and their magnetizations at 10 K are measured as functions of applied fields (ESI, Fig. S7†). For comparison, the saturation magnetizations of the LMO and LCO single layers are also shown in Fig. 4b. The magnetization of the LMO layer in SLs is close to that of its single layer counterpart whereas, unexpectedly, the LCO layer in SLs is significantly lower than the LCO single layer in magnetization (green line in Fig. 4b). This phenomenon cannot be ascribed to the effect of interlayer atomic diffusion. As revealed by the electron-energy-loss spectroscopy analysis, the thickness of this interfacial layer is in the order of ~1 nm (not shown). Considering the fact that each LCO layer is sandwiched between two LMO layers, the total thickness of the interfacial layer will be ~2 nm. Even if the interfacial layer yields null magnetic signals, the magnetization will be $(t_2 - 2)/t_2 \times M\mu_B$/Co, where M is the magnetization of the LCO single layer. As shown by the olive line in Fig. 4b, it is still significantly greater than the experimental values especially for the SLs with thick LCO layers. This result reveals the difference of the LCO in SLs form its single layer counterpart.

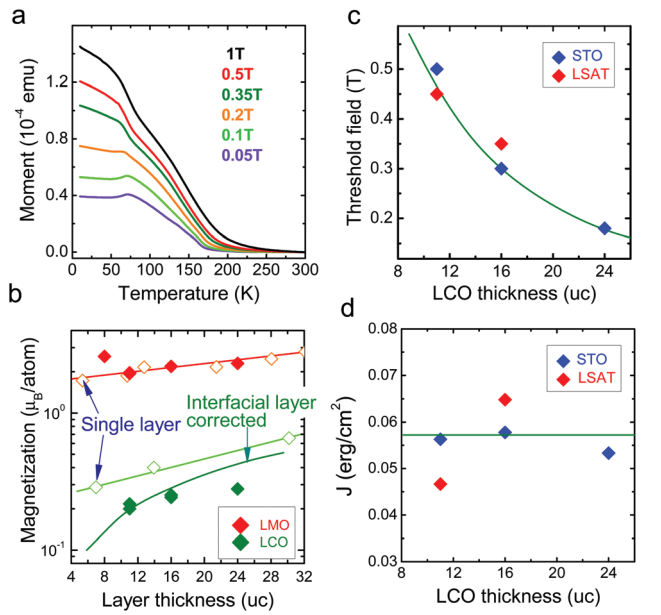

Fig. 4 (a) Thermomagnetic curves of $[LMO(11)/LCO(16)]_5$/STO, measured under different applied fields in field-cooling mode. (b) Saturation magnetization of the LMO and LCO layers in the SLs (solid symbols), deduced from the M–T curves obtained under a field of 1 T. Empty red and green symbols represent the results of the LMO and LCO single layers, respectively; dark green curve is the magnetization of the LCO single layer after subtracting a 2 nm thick interfacial layer. (c) Threshold field for magnetization reversion as a function of the layer thickness of LCO. Different colors mark the results for the SLs on different substrates. Solid line is a guide for the eye. (d) Exchange coupling energy as a function of the layer thickness of LCO. Different colors mark the results for the SLs on different substrates. Solid line is a guide to the eye.

Since thick LCO layers have large magnetic moments, their spin direction should be more easily reversed by a magnetic field. As shown in Fig. 4c, as t_2 grows from 11 uc to 24 uc, the threshold field for spin flip (H_{ST}), defined by the field where the magnetization reduction begins to reverse, decreases monotonically from ~0.50 T to ~0.18 T. Based on a simple formula $J = H_{ST}M/n$, we can calculate the interlayer coupling energy from the data in Fig. 4b, and it is found to vary between +0.05 and +0.06 erg cm^{-2} (Fig. 4d), where J is the exchange coupling energy, n = 9 is the interface number of the SLs, and M is the magnetization of the LCO layer. Here the positive sign specifies the AFM nature of interlayer coupling. Notably, this exchange energy is in the same order as that of metallic multilayers, for which the AFM coupling is generated by the Ruderman–Kittel–Kasuya–Yosida (RKKY) interaction.[29]

In general, the interlayer coupling will manifest itself as an exchange bias that affects the magnetizing process of the SLs. In Fig. 5a we show the field dependence of the magnetization of $[LMO(24)/LCO(24)]_5$/LSAT, recorded at 10 K with in-plane fields. A wasp-waisted magnetization curve is obtained (thick solid line). The thin elongated wasp-waist is ascribed to LMO while the other two bellies to LCO. This is clear after decomposing the complex magnetic loop into two simple loops (olive

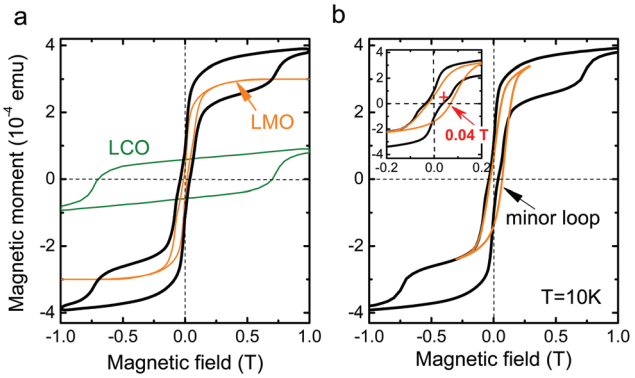

Fig. 5 (a) Field dependence of the magnetization of [LMO(24)/LCO(24)]$_5$/LSAT, recorded at 10 K with in-plane fields (thick curve). It can be decomposed into two independent loops associated with LMO and LCO, respectively (thin solid curves). (b) A comparison of the main magnetic loop and the minor loop that is obtained by saturating the sample under a field of +3 T and then a cycling magnetic field along the path of +0.25 T → −0.25 T → +0.25 T. Inset plot: a close view of the minor loop. Red cross here marks the center of the minor loop.

and orange thin curves). Fig. 5b and its inset plot show the minor loop, recorded by saturating the sample under a field of +3 T and then cycling along the paths of +0.25 T → −0.25 T → +0.25 T. As denoted by a red cross mark, the center of the minor loop deviates from the origin by a field of ~0.04 T. This result indicates a positive exchange bias, confirming the AFM nature of the interlayer coupling.

As is well established, Mn^{3+} in LMO is a high spin ion, with three t_{2g} electrons and one e_g electron. Different from Mn^{3+}, Co^{3+} is a LS ion in unstrained LCO or partially a high spin ion in tensile LCO film. The occurrence of interlayer coupling implies that at least parts of Co^{3+} ions in the SLs are in a HS or IS state, forming magnetic exchange with adjacent Mn ions.

AFM interlayer coupling has been reported for the LSMO/SRO SLs[8] and bilayers.[9] For the LSMO/SRO structure electronic transport is a prerequisite for establishing a FM order and thus an AFM interlayer coupling since the magnetic interaction is double exchange (for LSMO) or itinerant ferromagnetic exchange (for SRO). In contrast, both LMO and LCO are insulators, and their magnetism mainly stems from superexchange. This is the main difference between LMO/LCO and LSMO/SRO. Our work reveals that an AFM interlayer coupling can also occur between insulating perovskites, thus extending the spin engineering to the perovskites beyond itinerant FM oxides.

In addition to AFM interlayer coupling, so far we have observed phenomena that are unique for LCO-based SLs, *i.e.*, interface-induced parallel lattice modulation and substantially reduced magnetization. In the LCO layer of our SLs, dark stripes are parallel to the interface, and appear every two columns rather than every three columns as in a single layer.[24,25] This implies a high instead of a low magnetic moment since magnetization will grow in proportion to the density of dark stripes according to the work of Lan *et al.*[28] As discussed above, the low magnetization of the LCO layer in SLs cannot be simply ascribed to reduced interfacial magnetism. It could be an indication of the occurrence of a complex spin texture in the LCO layer. At first, the spin structure could be canted or spiral if strongly competing mechanisms coexist, exhibiting a reduction in net magnetization. Also, an antiparallel alignment of magnetic moments is possible for the Co^{3+} ions in neighboring dark stripes, leading to a magnetic counteraction. Since the LCO layer is sandwiched between two parallel LCO–LMO interfaces, within which any long-range magnetic order must satisfy a boundary condition, *i.e.*, AFM interlayer coupling. Additionally, a charge transfer from Mn^{3+} to Co^{3+} could take place, modifying not only ion valence but also orbital population. These boundary effects may extend well into the inner part of the LCO layer, resulting in a unusual spin texture.

To obtain a deep insight into the spin structure of the LMO/LCO SLs, we performed *ab initio* calculations on the magnetic structure of [LMO(4 uc)/LCO(t_2)]$_5$/STO with t_2 = 5 uc and 9 uc within the framework of density functional theory. The spin state of Co^{3+} may be sensitive to both lattice strain and interlayer coupling because of its comparable Hund's rule coupling and crystal field splitting. The effect of lattice strains has been well established for the LCO layer, whereas the effect of interlayer coupling remains elusive. Considering the fact that the interlayer coupling could be strong only within a distance of several monolayers from the interface (for manganite heterostructures, for example, the effect of oxygen octahedral coupling is significant within ~7 uc from the interface[30]), we set the layer thickness of LCO to 9 uc which is thicker than 7 uc. We also adopted a model with a layer thickness of 5 uc for comparison. Different from Co^{3+}, the spin state of Mn^{3+} is much more stable, insensitive to interlayer coupling. To save computation time, we set the layer thickness of LMO to 4 uc.

The projector augmented plane-wave (PAW) pseudo-potentials were used, as implemented in the Vienna *ab initio* Simulation Package (VASP). To reliably describe exchange and correlation interactions, the generalized gradient approximation GGA+U method was employed, adopting the effective Hubbard parameter of U_{eff} = 3.9 eV for Co in LCO[17,31] and U_{eff} = 3.0 eV for Mn in LMO.[32] The in-plane lattice constant was set to that of STO (SLs share the same in-plane lattice parameter with the substrate as is evidenced by RSM images), and the out-of-plane lattice constants of LMO and LCO were deduced from the XRD and STEM data. The out-of-plane La–La bond length is 4.26 Å in dark stripes and 3.28 Å elsewhere for the LCO layer and 3.94 Å for the LMO layer. The superstructure was so built that the dark stripe forms every two rows, and the first dark stripe appears in the row in proximity of the LMO layer as revealed by the HAADF image. Through adjusting the coordinates of the Mn, Co, and O atoms while fixing the atomic position of La, we obtained a stable crystal structure with a minimal total energy. For the SLs, thus obtained electronic and magnetic structures were calculated.

The superstructure for the density functional theory calculations is shown in Fig. 6a. Fig. 6b presents the projected

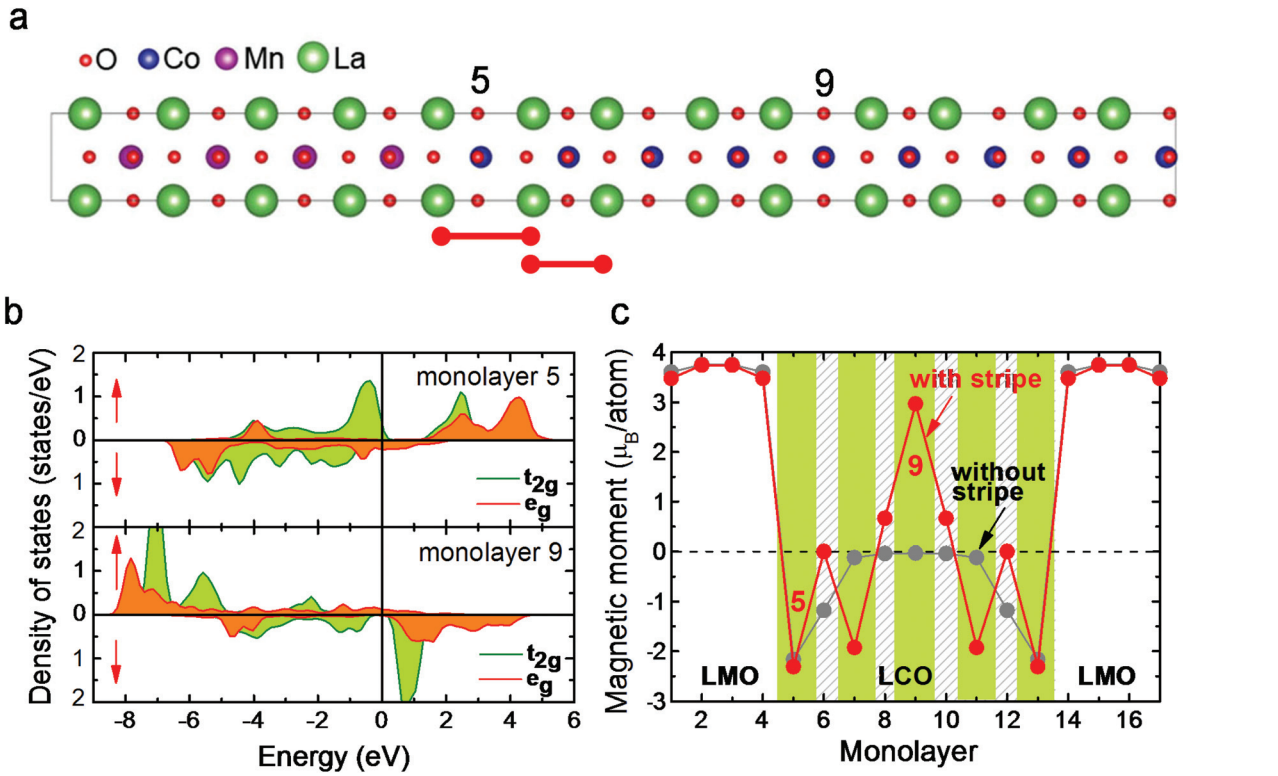

Fig. 6 (a) Superstructure for density functional theory calculations for the LMO(4 uc)/LCO(9 uc) SL. Two types of La–La bond lengths have been adopted in the LCO layer to simulate structure modulation. The underneath line segments schematically show the two La–La bond lengths. (b) Projected density of states for 3d orbitals at a Co^{3+} site of the fifth and ninth monolayers in the LCO layer of the SL. Dashed line marks the Fermi energy. Positive and negative densities of states represent the spin up and spin down states, respectively. (c) Calculated local magnetic moments as functions of the coordinates of Mn or Co. Green and grey backgrounds mark the LCO layer in the SLs (green: dark stripes). Labels in the figure denote the numbers of the CoO_2 columns.

density of states for the 3d orbitals at the Co^{3+} site of the fifth and ninth CoO_2 monolayers. The former is the nearest neighbor of LMO and the latter is at the middle location of the LCO layer. At first glance, the spin state of Co^{3+} strongly depends on the distance from the interface. The most populated state is the spin down state at the interface and the spin up state in the middle of the LCO layer. To get a clear picture of the magnetic structure, in Fig. 6c we show the spatial distribution of magnetic moments. The magnetic moments of the Mn ions form a simple FM order, with an average magnitude of $\sim 3.61\mu_B$/Mn. This value is slightly smaller than the expected $\sim 4.00\mu_B$/Mn for Mn^{3+} but considerably larger than the measured $\sim 2.33\mu_B$/Mn (Fig. 4b). The decreased magnetization of Mn^{3+} could be ascribed to interfacial effects, defects or off-stoichiometry of the LMO layer that have been ignored by the present calculation. In contrast, the spin structure of the LCO layer is much more complex. The Co ion in the column neighboring the LMO exhibits a magnetic moment of about $-2.31\mu_B$/Co, antiparallel to that of Mn. As the distance from the interface increases, fascinatingly, the magnetic moments oscillate in both magnitude and direction, forming a wave-like spin texture. The maximal magnetic moment is about $+2.97\mu_B$/Co, gained by the Co ion in the middle CoO_2 column of the LCO layer. The net magnetic moment is about $-0.46\mu_B$/Co, aligning against that of Mn ions. This is in fairly good agreement with experimental results ($-0.28\mu_B$/Co). Notably, sizable magnetic moments always appear in the CoO_2 columns in dark stripes (marked by light green strips in Fig. 6c), which is consistent with the reported results that the HS/IS Co ions locate along the dark stripes.[24,25,28] For comparison, we also calculated the spin structure for a model without structural modulation, and found that the magnetic moment is the highest at the interface and decays rapidly away from the interface, without any signatures of oscillation. The net magnetic moment is about $-0.78\mu_B$/Co, substantially larger than the experimental value. In the case of LMO(4 uc)/LCO(5 uc), we also obtained an AFM interlayer coupling though the magnetic oscillation is not as strong as that observed for LMO(4 uc)/LCO (9 uc) (not shown). In addition to the AFM order, these results support the spin texture characterized by antiparallel aligned rather than the canted or spiral spin structure, demonstrating the distinct effect of interlayer coupling.

LCO is featured by its spin state transition, and sometimes different spin state Co ions coexist in cobalt oxides, resulting in different exchange processes such as the double exchange between an IS Co^{3+} and a HS Co^{4+} as for $La_{0.7}Sr_{0.3}CoO_3$ [33] and the superexchange between two HS Co^{3+}, with the help of an intermediate LS Co^{3+} as for tensile LCO films.[17] Quantitative

analysis showed that the energies of the IS and HS states at 0 K are 22.5 meV and 124.6 meV, respectively, above that of the LS state.[18] This difference may be further reduced by cooperative structural distortions in these two spin states. As a consequence, the spin state of Co ions is very sensitive to external stimuli. This has been confirmed by thermal energy-induced or lattice strain-induced spin state transition. In addition to structural deformation, the magnetic exchange between the Co and Mn ions may also provide energy affecting the delicate balance between Hund coupling and crystal field splitting in LCO, stabilizing the HS or IS state. As reported, the exchange energy can be as high as ~18.3 meV for the transition metal oxides such as NiO.[34] This may explain why the first dark stripe usually forms along the LMO–LCO interface. As shown by the above theory calculations, Co ions in dark stripes have finite magnetic moments.

Compared with the FM/FM SLs, for which the magnetic structure in each layer remains simply FM since the magnetic exchange within each layer is robust, the wave-like spin structure in the LCO-based SLs is particularly interesting. This kind of spin structure will allow us to explore the hidden aspects of magnetic SLs. At first, the excitation and propagation of spin waves in this kind of SL could be considerably different from the conventional magnetic materials because of the distinct spatial spin oscillation. Second, the spin texture is sensitive to an external field, undergoing a switching between different states. As a result, the transport behavior of spin current and the efficiency of spin-to-charge conversion could be feasibly tunable.

3. Summary

Interlayer coupling and its effect on LCO in the LMO/LCO superlattices, which is featured by a tunable spin state, have been systematically studied. The LCO layer is found to show not only a long range magnetic order with usually low magnetization, which suggests a complex spin structure in this layer, but also an AFM coupling with a LMO layer. Moreover, the AFM spin alignment is subject to the modification of a magnetic field, transiting into a parallel arrangement above the fields of 0.5 T. Density functional theory calculation shows a spatial oscillation of magnetic moment within the LCO layer, resulting in a net magnetic moment that is antiparallel to that of the LMO layer. The present work shows the possibility of tuning a spin texture through interfacial engineering for the complex oxides whose spin state is jointly determined by strongly competing mechanisms.

Acknowledgements

This work has been supported by the National Basic Research of China (2013CB921700, 2016YFA0300701), the National Natural Science Foundation of China (11520101002, 51590880, 11374348, 11134007, 11574376, and 11574366) and the Key Program of the Chinese Academy of Sciences.

References

1 H. Y. Hwang, Y. Iwasa, M. Kawasaki, B. Keimer, N. Nagaosa and Y. Yokura, *Nat. Mater.*, 2012, **11**, 103.
2 N. Reyren, S. Thiel, A. D. Caviglia, L. F. Kourkoutis, G. Hammeri, C. Richter, C. W. Schneider, T. Kopp, A. S. Ruetschi, D. Jaccard, M. Gabay, D. A. Muller, J. M. Triscone and J. Mannhart, *Science*, 2007, **317**, 1196–1199.
3 A. D. Caviglia, S. Gariglio, N. Reyren, D. Jaccard, T. Schneider, M. Gabay, S. Thiel, G. Hammerl, J. Mannhart and J. M. Triscone, *Nature*, 2008, **456**, 624–627.
4 A. Brinkman, M. Huijben, M. Van Zalk, J. Huijben, U. Zeitler, J. C. Maan, W. G. Van der Wiel, G. Rijnders, D. H. A. Blank and H. Hilgenkamp, *Nat. Mater.*, 2007, **6**, 493–496.
5 J. S. Lee, Y. W. Xie, H. K. Sato, C. Bell, Y. Hikita, H. Y. Hwang and C. C. Kao, *Nat. Mater.*, 2013, **12**, 703–706.
6 A. Joshua, J. Ruhman, S. Pecker, E. Altman and S. Ilani, *Proc. Natl. Acad. Sci. U. S. A.*, 2013, **110**, 9633–9638.
7 A. Sadoc, B. Mercey, C. Simon, D. Grebille, W. Prellier and M. Lepetit, *Phys. Rev. Lett.*, 2010, **104**, 046804.
8 M. Ziese, I. Vrejoiu, E. Pippel, P. Esquinazi, D. Hesse, C. Etz, J. Henk, A. Ernst, I. V. Maznichenko, W. Hergert and I. Mertig, *Phys. Rev. Lett.*, 2010, **104**, 167203.
9 X. Ke, L. J. Belenky, V. Lauter, H. Ambaye, C. W. Bark, C. B. Eom and M. S. Rzchowski, *Phys. Rev. Lett.*, 2013, **110**, 237201.
10 J. Chakhalian, J. W. Freeland, G. Srajer, J. Strempfer, G. Khaliullin, J. C. Cezar, T. Dalgliesh, R. Dalgliesh, C. Bernhard, G. Cristiani, H. U. Habermeier and B. Keimer, *Nat. Phys.*, 2006, **2**, 244–248.
11 J. Chakhalian, J. W. Freeland, H. U. Habermeier, G. Cristiani, G. Khaliullin, M. van Veenendaal and B. Keimer, *Science*, 2007, **318**, 1114–1117.
12 D. K. Satapathy, M. A. Uribe-Laverde, I. Marozau, V. K. Malik, S. Das, T. Wagner, C. Marcelot, J. Stahn, S. Bruck, A. Ruhm, S. Macke, T. Tietze, E. Goering, A. Frano, J. H. Kim, M. Wu, E. Benckiser, B. Keimer, A. Devishvili, B. P. Toperverg, M. Merz, P. Nagel, S. Schuppler and C. Bernhard, *Phys. Rev. Lett.*, 2012, **108**, 197201.
13 M. Gibert, P. Zubko, R. Scherwitzl, J. Íñiguez and I. Triscone, *Nat. Mater.*, 2012, **11**, 195–198.
14 S. Yamaguchi, Y. Okimoto, H. Taniguchi and Y. Tokura, *Phys. Rev. B: Condens. Matter*, 1996, **55**, R2926–R2929.
15 T. Saitoh, T. Mizokawa, A. Fujimori, M. Abbate, Y. Takeda and M. Takano, *Phys. Rev. B: Condens. Matter*, 1997, **55**, 4257–4266.
16 D. Fuchs, C. Pinta, T. Schwarz, P. Schweiss, P. Nagel, S. Schuppler, R. Schneider, M. Merz, G. Roth and H. von Lohneysen, *Phys. Rev. B: Condens. Matter*, 2007, **75**, 144402.
17 H. Seo, D. Posadas and A. A. Demkov, *Phys. Rev. B: Condens. Matter*, 2002, **86**, 014430.
18 K. Asai, O. Yokokura, M. Suzuki, T. Naka, T. Matsumoto, H. Takahashi, N. Mori and K. Kohn, *J. Phys. Soc. Jpn.*, 1997, **66**, 967–970.

19 J. Baier, S. Jodlauk, M. Kriener, A. Reichl, C. Zobel, H. Kierspel, A. Freimuth and T. Lorenz, *Phys. Rev. B: Condens. Matter*, 2003, **71**, 014443.
20 Y. Kanamori, H. Matsueda and S. Ishihara, *Phys. Rev. Lett.*, 2011, **107**, 167403.
21 E. O. Wollan and W. C. Koehler, *Phys. Rev.*, 1955, **100**, 545–563.
22 H. S. Kim and H. M. Christen, *J. Phys.: Condens. Matter*, 2010, **22**, 146007.
23 S. Dong, R. Yu, S. Yunoki, G. Alvarez, J.-M. Liu and E. Dagotto, *Phys. Rev. B: Condens. Matter*, 2008, **78**, 201102.
24 W. S. Choi, J. H. Kwon, H. Jeen, J. E. Hamann-Borrero, A. Radi, S. Macke, R. Sutarto, F. Z. He, G. A. Sawatzky, V. Hinkov, M. Kim and H. N. Lee, *Nano Lett.*, 2012, **12**, 4966–4970.
25 N. Bišskup, J. Salafranca, V. Mehta, M. P. Oxley, Y. Suzuki, S. J. Pennycook, S. T. Pantelides and M. Varela, *Phys. Rev. Lett.*, 2014, **112**, 087202.
26 A. N. Petrov, O. F. Kononchuk, A. V. Andreev, V. A. Cherepanov and P. Kofstad, *Solid State Ionics*, 1995, **80**, 189–199.
27 Q. Huang, A. Santoro, J. W. Lynn, R. W. Erwin, J. A. Borchers, J. L. Peng and R. L. Greene, *Phys. Rev. B: Condens. Matter*, 1997, **55**, 14987–14999.
28 Q. Q. Lan, X. Shen, H. W. Yang, H. R. Zhang, J. Zhang, X. X. Guan, Y. Yao, Y. G. Wang, R. C. Yu, Y. Peng and J. R. Sun, *Appl. Phys. Lett.*, 2015, **107**, 242404.
29 X. Zhang, Y. Zhang and J. W. Cai, *J. Appl. Phys.*, 2015, **118**, 143903.
30 Z. Liao, M. Huijben, Z. Zhong, N. Gauquelin, S. Macke, R. J. Green, S. van Aert, J. Verbeeck, G. van Tendeloo, K. Held, G. A. Sawatzky, G. Koster and G. Rijnders, *Nat. Mater.*, 2016, **15**, 425–431.
31 Y. Wang, Z. J. Wang, Z. Fang and D. Dai, *Phys. Rev. B: Condens. Matter*, 2015, **91**, 125139.
32 Q. Zhang, S. Dong, B. L. Wang and S. Yunoki, *Phys. Rev. B: Condens. Matter*, 2012, **86**, 094403.
33 D. Fuchs, M. Merz, P. Nagel, R. Schneider, S. Schuppler and H. von Lohneysen, *Phys. Rev. Lett.*, 2013, **111**, 257203.
34 R. Shanker and R. A. Singh, *Phys. Rev. B: Solid State*, 1973, **7**, 5000–5005.

